Polarization properties of Raman scattering by surface phonon polaritons in GaAsP nanowires

OPEN ACCESS
IOP Publishing
Journal of Physics D: Applied Physics
J. Phys. D: Appl. Phys. **54** (2021) 475109 (11pp)
https://doi.org/10.1088/1361-6463/ac2400

Polarization properties of Raman scattering by surface phonon polaritons in GaAsP nanowires

Sergey I Rybchenko[1,*], Sarfraz Ali[1], Yunyan Zhang[2,3,*] and Huiyun Liu[2]

[1] Department of Engineering, University of Hull, Hull HU67RX, United Kingdom
[2] Department of Electronic and Electrical Engineering, University College London, London WC1E 7JE, United Kingdom
[3] Department of Physics, Universität Paderborn, Warburger Straße 100, 33098 Paderborn, Germany

E-mail: s.i.rybchenko@hull.ac.uk and yunyan.zhang@uni-paderborn.de

Received 8 June 2021, revised 30 August 2021
Accepted for publication 6 September 2021
Published 16 September 2021

Abstract

Strong resonant enhancement of Raman scattering on photonic resonance was observed in GaAsP semiconductor nanowires. The enhancement allowed for detailed studies of the surface phonon polariton (SPhP) scattering peak on individual nanowires. In particular, for the first time, the effect of the nanowire cross section shape on SPhP properties has been investigated. It was found that the cross section flattening induces a strong polarisation and a spectral shift of SPhPs supported by such nanowire. The assisting numerical simulations allowed to link the induced polarisation effect to a splitting of the resonant HE11 mode in the flattened nanowire. The observed spectral shift of SPhP has been also theoretically reproduced in elliptical approximation for the flattened cross section. The obtained results pave a ground for engineering of SPhP polarisation response and accurate spectral control of SPhPs in applications utilising the nanowire morphology.

Supplementary material for this article is available online

Keywords: semiconductor nanowires, surface phonon polaritons, Raman scattering, dielectric photonic resonances, surface sensors

(Some figures may appear in colour only in the online journal)

1. Introduction

Surface phonon polaritons (SPhPs) are quasiparticle excitations associated with surfaces and interfaces of non-centrosymmetric dielectric crystalline materials [1, 2]. They represent mixed optical-phonon—photon states, which can be obtained as solutions of Maxwell's equations for the frequency range where the real part of dielectric permittivity is negative. For natural crystalline dielectrics this range is found in far infra-red (IR) spectral window. The surface nature of SPhPs makes them sensitive to the dielectric permeability of surrounding environment [1], which creates potential for diagnostics of surface dielectric properties [3]. Arising from far-IR frequency window, SPhPs spectrally overlap with molecular vibrations and hence they have been considered for developing ultrasensitive molecular spectroscopy [4, 5] and even for alteration of molecular chemical activity [6–8]. Recently there have been a sharp increase of interest to SPhPs as an attractive platform for IR miniaturised photonic circuits due to the extremely high compression of free-space

* Authors to whom any correspondence should be addressed.

wavelength corresponding to far-IR photons [2, 9–11] at relatively low losses that can be achieved with SPhPs. Thermal emission is another rapidly growing area for SPhP applications. Distance, spectral, polarisation, and angular control of thermal emitters-absorbers has been demonstrated via coupling of far-field [12] or near-field [13, 14] radiation to SPhPs. In addition, energy routing and focussing by means of SPhP has been predicted [15]. SPhP based photonic control of thermal emission has allowed for improvement of traditional applications such as thermophotovoltaics [13, 14] and also lead to emerging application opportunities such as daytime radiative cooling [16] and night-time photovoltaics generation [17]. These new application areas created a demand for SPhP characterisation methods, which would allow for accurate evaluation of the energy spectrum, polarisation, lifetime and other properties of SPhP excitations in supporting nanostructures. This includes a demand for novel efficient SPhP sources and detectors, especially in on-chip integrable format [18].

Raman scattering is a powerful method for characterisation of variety of quasiparticle excitations in dielectrics [19–22], including SPhPs. SPhPs dispersion and polarization properties has been successfully evaluated by Raman spectroscopy for bulk crystals [23–25] and thin films [26–28]. But when it comes to other popular morphologies such as nanowires, the examples of SPhP characterisation are rare and often related to Raman scattering from the nanowire assemblies [29–35] rather than from isolated nanowires [36–38].

Recently we have demonstrated [39] the amplification of Raman scattering by SPhPs on HE11 photonic resonance in GaAs nanowires, establishing the required experimental conditions. In this paper, we have reproduced the resonance amplification effect on GaAsP nanowires and utilised it for detailed characterisation of polarisation properties of SPhPs in nanowires of different cross section shape.

2. Methods

2.1. Nanowire growth

$GaAs_{1-x}P_x$ NWs were fabricated by a solid-source molecular-beam epitaxy (MBE) with a solid Ga source and As4 and P2 cracker cells. 380 μm thick B-doped silicon (111) substrates were used in the experiments. The growth parameters including Ga beam equivalent pressure, V/III flux ratio, P/(As + P) flux ratio, substrate temperature and growth duration of 1.12×10^{-7} Torr, 50, 0.12, ~640 °C, and 1 h, respectively. The phosphorus content was determined ($x = 0.28 \pm 0.01$) by energy dispersive x-ray (EDX) analysis (available on transmission electron microscope (TEM)) and further confirmed via tabulated Raman parameters (see supplementary note S2 (available online at stacks.iop.org/JPD/54/475109/mmedia)).

2.2. Sample processing

For obtaining NWs detached from a substrate (cut-off NWs), the as-grown sample was sonicated in ethanol using an ultrasonic bath (60 W) for 5 min. The obtained dispersion of NWs in ethanol has been subsequently applied in drops on Si/SO_x substrate or TEM lacey carbon grids to deposit the cut-off NWs. The sonicated substrates ('shaved' substrates) have been removed from the ethanol and dried in nitrogen gas flow. The other method of local 'shaving-off' NWs was also used. In this method, the local stamping of the as-grown sample with non-sticky gel was used, which allowed to remove the NWs but leave the clusters in place (see figure S2).

2.3. Raman measurements

All Raman measurements have been conducted at room temperature using LabRAM (HORIBA) spectrometer equipped with confocal microscope, Peltier-cooled CCD detector, and HeNe laser ($\lambda = 632.8$ nm). The microscope is equipped with precise X–Y scanning sample stage (min step of 0.2 μm), piezo focus lens positioner, and ×100 dry objective lens (NA = 0.92). Excitation laser power was adjusted using a built-in set of reflective neutral density filters. Excitation laser power level of 12 μW was selected. Polarisation unanalysed Stokes–Raman spectra ($z(x'x' + x'y')\bar{z}$, or 'unanalysed' spectra) were normally collected except where crossed ($z(x'y')\bar{z}$) or parallel ($z(x'x')\bar{z}$) polarisation is explicitly noted. For polarisation control, the half-wave plate and absorptive polarizer have been used. For a polarisation diagram, a series of unanalysed Raman spectra were taken at different in-plane polarisation angles covering 180° range and the diagram was constructed showing the integral intensity of the Raman spectrum as function of the in-plane polarisation angle. The obtained results were corrected for the spectrometer instrumental polarisation function.

2.4. Numerical simulation

The numerical simulations were performed using the finite element method implemented in commercial COMSOL Multiphysics software. The excitation field distributions and mode dispersions were calculated by solving Maxwell equations in the frequency domain for a suspended finite-length NW and an infinite non-absorbing NW respectively. The finite-length NW was simulated as a 4 μm/2 μm long cylinder or truncated cone suspended in a large cavity bounded by artificial perfectly-absorbing walls implemented using perfectly matched layer feature of COMSOL software. For the truncated cone shape, the top diameter was kept at half of the pedestal diameter. Plane wave excitation has been employed unless mentioned otherwise. Material optical parameters for GaAsP have been taken from [40–42].

3. Results and discussion

3.1. Hot spots in Raman mapping

$GaAs_{1-x}P_x$ nanowires were fabricated by MBE with self-catalysed mode on silicon substrates. They have typical characteristics for the chosen growth method which was described in details in earlier publications [43, 44], and have an average

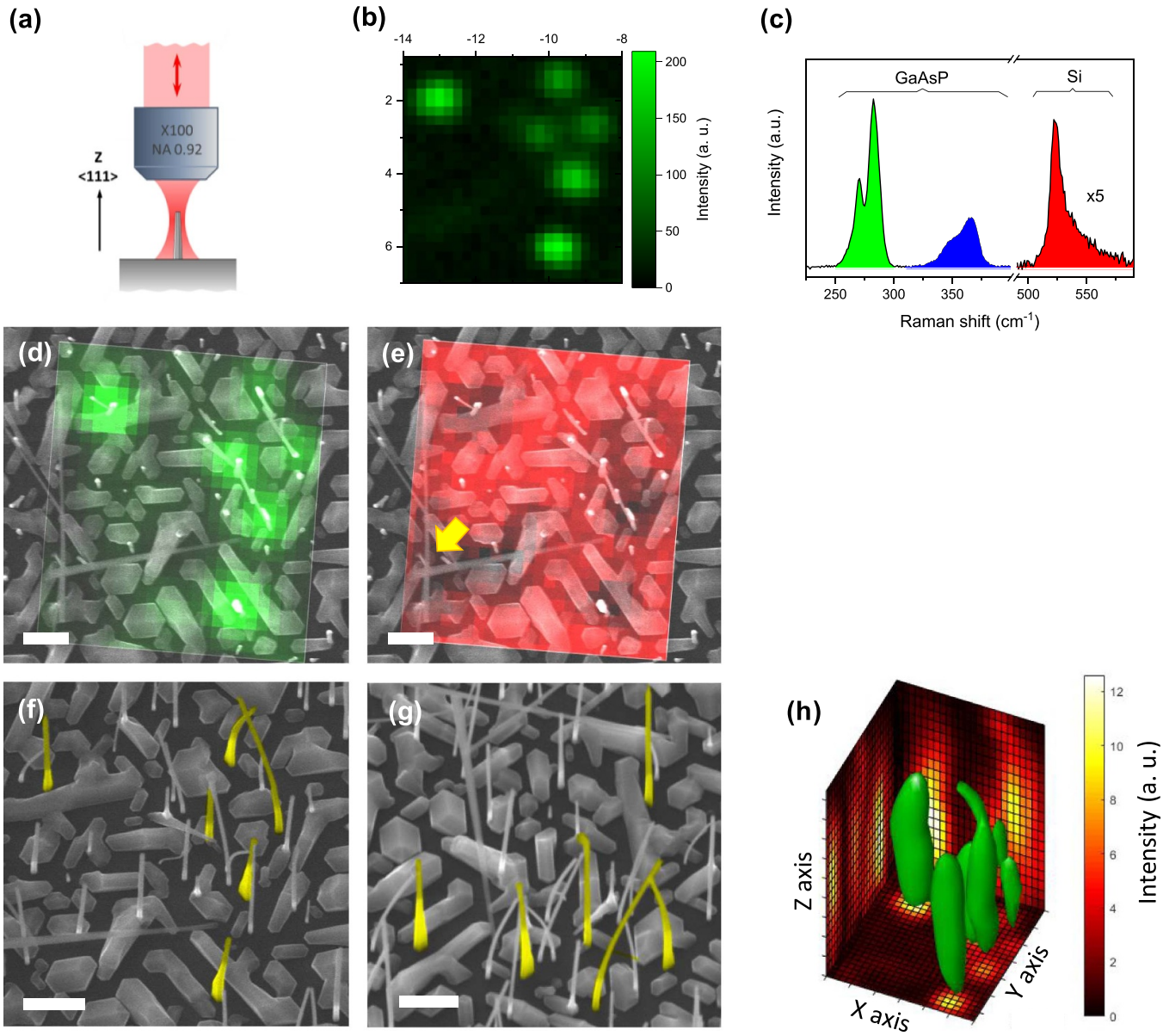

Figure 1. Raman mapping of as-grown nanowire sample. (a) Schematics of scattering geometry. (b) Integral intensity map of GaAsP phonon band for group of six hot spots. Scale is in μm. (c) Typical Raman spectrum of the hot spot showing phonon bands of GaAsP (green and blue) and Si substrate (red). Figures (d) and (e) composite maps of GaAsP (green) and Si (red) Raman intensity distribution for the same group of hot spots. Yellow arrow in (e) indicates two crossed spike-like NWs. Figures (f) and (g) SEM images of the area in (d), (e) taken at inclination to the down (10°) and right (15°) side, respectively. NWs highlighted in yellow are related to the six brightest green spots in (b) and (d). Scale bar in (d)–(g) is 1 μm. (h) 3D map of the same hot spot group as in (b). 3D Raman data of GaAsP phonon band (green-colour isosurface at 40% of max signal is smoothed for clarity) shown together with maximum intensity projections in *x, y*, and *z* directions. Scale division is 1 μm for all axes. Bottom of *z* scale is at 0.5 μm below the substrate level.

diameter of 50–70 nm and length of 4–6 μm as confirmed by SEM and TEM images (figure S1). A small percentage of nanowires are with a spike-like morphology grown at angle of $\sim$35° to the substrate (figure S1(a)). At the bottom level of nanowires, there is a layer of aggregates of thickness of 300–500 nm, known as 'parasitic clusters'. The phosphorus content $x = 0.28 \pm 0.01$ has been established using EDX analysis combined with TEM.

Raman mapping of as-grown GaAsP nanowire samples taken in backscattering geometry (see figure 1(a)) revealed strong highly localised maxima (hot spots), as shown in figure S3. They have a signal intensity exceeding signal from the individual cut-off nanowires (see note S1) by two orders of magnitude. The density of these maxima varies across the sample, but it is always less than 10% of the average NW density. This Raman hot spots phenomenon is similar to that observed on GaAs nanowire samples [39]. However, the intensity of the hot spots tends to be higher in GaAsP samples, which can be explained by the lower laser light absorption coefficient in this material. Lower absorption also leads to lower laser damage, allowing for multiple scanning of the same hot spot. Zooming into figures S3(b) and 1(b) shows

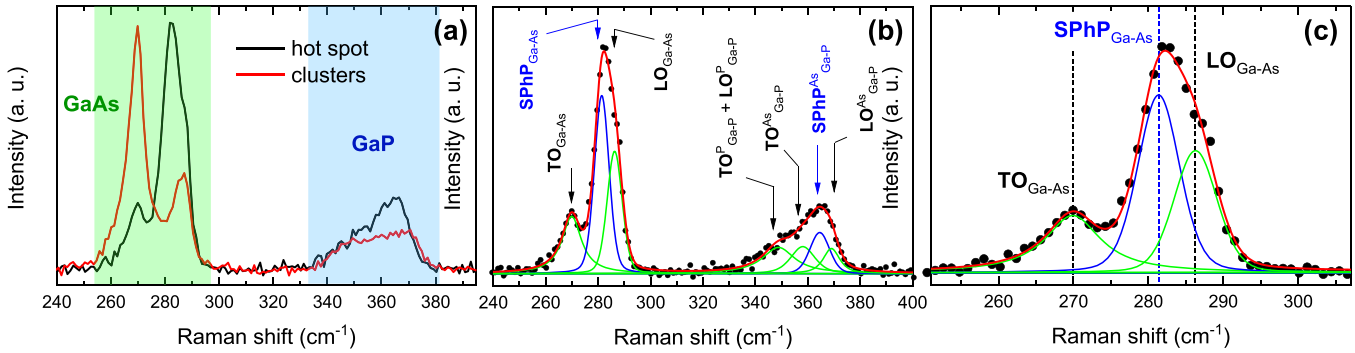

Figure 2. Unanalysed Raman spectra obtained on as-grown samples. (a) Normalised spectra of hot spot and clusters. GaAs and GaP phonon bands indicated. (b) Fitting of the hot-spot spectrum from (a) by Voigt peak functions (green and blue curves). Symbols are experimental data points and red curve is the resulting fit. Peak assignment is shown. (c) Same as (b) for GaAs phonon band only.

the averaged Raman map obtained from three subsequent scans, illustrating the repeatability of mapping (see more in figure S3(c)). A representative Raman spectrum collected from the hot spot area (figure 1(c)) shows GaAsP phonon peaks grouped into two bands related to the parent compounds of GaAs and GaP, in agreement with earlier reports for bulk [45, 46] and nanowire samples [47]. The integral intensity of the strongest GaAsP phonon band (green, GaAs-related) has been used for mapping in figures 1(b) and (d). In addition, the spectrum in figure 1(c) also shows a background peak from the silicon substrate (∼520 cm^{-1}). The integral intensity of this peak has been mapped in figure 1(e). The composite images in figures 1(d) and (e) show GaAsP and Si components of the Raman map overlaid on top-view SEM image of the same area of the sample. The hot spots from the green GaAsP map (figure 1(d)) appear as dark spots on the red Si map (figure 1(e)), indicating an efficient absorption of the laser emission at the hot-spot locations. Correlated study of the Raman maps and corresponding SEM images allowed to establish that the hot spots are related to individual nanowires characterized by larger than average diameter (cross-section size) and pronounced tapering. The geometrical parameters of these thicker NWs were obtained from their SEM images taken at inclined view to the sample's normal (figures 1(f) and (g)). Averaging over 13 of such hot spots from different sampling areas, the mean diameter of hot-spot nanowires at half-height level is 118.5 ± 20 nm whereas their length-averaged taper is within 0.3°–0.7° range. This taper corresponds to ≈2 times diameter variation over the typical nanowire length of 5 μm. The hot-spot nanowires also often have a flattened blade-like shape characterized by an elongated cross-section (figures 1(f) and (g)).

For thick spike-like nanowires (see figure S1(a)) grown at low angles to the sample surface (indicated by yellow arrow in figures 1(e) and S3(d)), the prominent Raman signal is not observed, despite the fact that their geometrical parameters (cross-section size, taper and length) are similar to those nanowires with the hot spots.

On the other hand, these spikes appear as dark areas on the silicon map (figures 1(e) and S3(d)), indicating local shadowing of the substrate due to strong absorption (or scattering) of the laser light on these objects similar to that on the hot spots. This implies that the standing up orientation (ensuring a backscattering geometry along the nanowire axis) is a principal condition for obtaining a strong Raman signal in the thick tapered nanowires, as suggested in [39].

3D Raman mapping of the hot spots shown in figures 1(h) and S3(f) allow for assessment of the intensity variation along vertical (z) direction. It can be seen that centres of mass of green isosurfaces are lifted above the substrate level. The linked maximum intensity projections in X and Y directions show that the maximum of the Raman signal is often located at 2 and 3 μm above the substrate level, i.e. at the mid-height range of the nanowire. Similar feature was observed for hot spots in GaAs samples [39], where it was related to the effect of tapering on the excitation light intensity distribution. The 3D map also indicates that the Raman signal from the underlayer of thick clusters typically present in our samples (figure S1) is much weaker than that of the hot spots, despite the larger volume of material involved in the clusters. That was directly confirmed by mapping of the 'shaved' samples (see note S1 and figure S2).

3.2. *Raman spectra of hot spots*

When comparing the hot-spot Raman spectrum with that of clusters (figure 2(a)), strong extra peak is present in spectrum of the hot spot in between $LO_{Ga–As}$ and $TO_{Ga–As}$ (GaAs-band) in addition to 'bulk' LO_{Ga-As} and $TO_{Ga–As}$ modes, mimicking the SPhP peak appearance in pure GaAs samples [39]. The separation of this $SPhP_{Ga–As}$ peak from $LO_{Ga–As}$ is not that obvious due to the narrower LO_{GaAs}–TO_{GaAs} splitting (6.5 cm^{-1} against 13 cm^{-1} in pure GaAs) and larger peaks broadening in the alloy compound (7–9 cm^{-1} against 3–4 cm^{-1} in pure GaAs). However, it can be accurately established via peak fitting (figures 2(b) and (c)) assuming that $LO_{Ga–As}$ and $TO_{Ga–As}$ peak frequencies are fixed within the ranges obtained from the fitting of the clusters and cut-off nanowires spectra (figures S5(a), (c) and note S2). Following this procedure, we have found that $SPhP_{Ga–As}$ peak position varies within 281.5–284 cm^{-1} range, while its width (FWHM) is 8.5 ± 0.7 cm^{-1}. The peak width value is close to that of the 'bulk' $LO_{Ga–As}$ and $TO_{Ga–As}$ modes. This is different from the SPhP peak characteristics in GaAs nanowires, where the

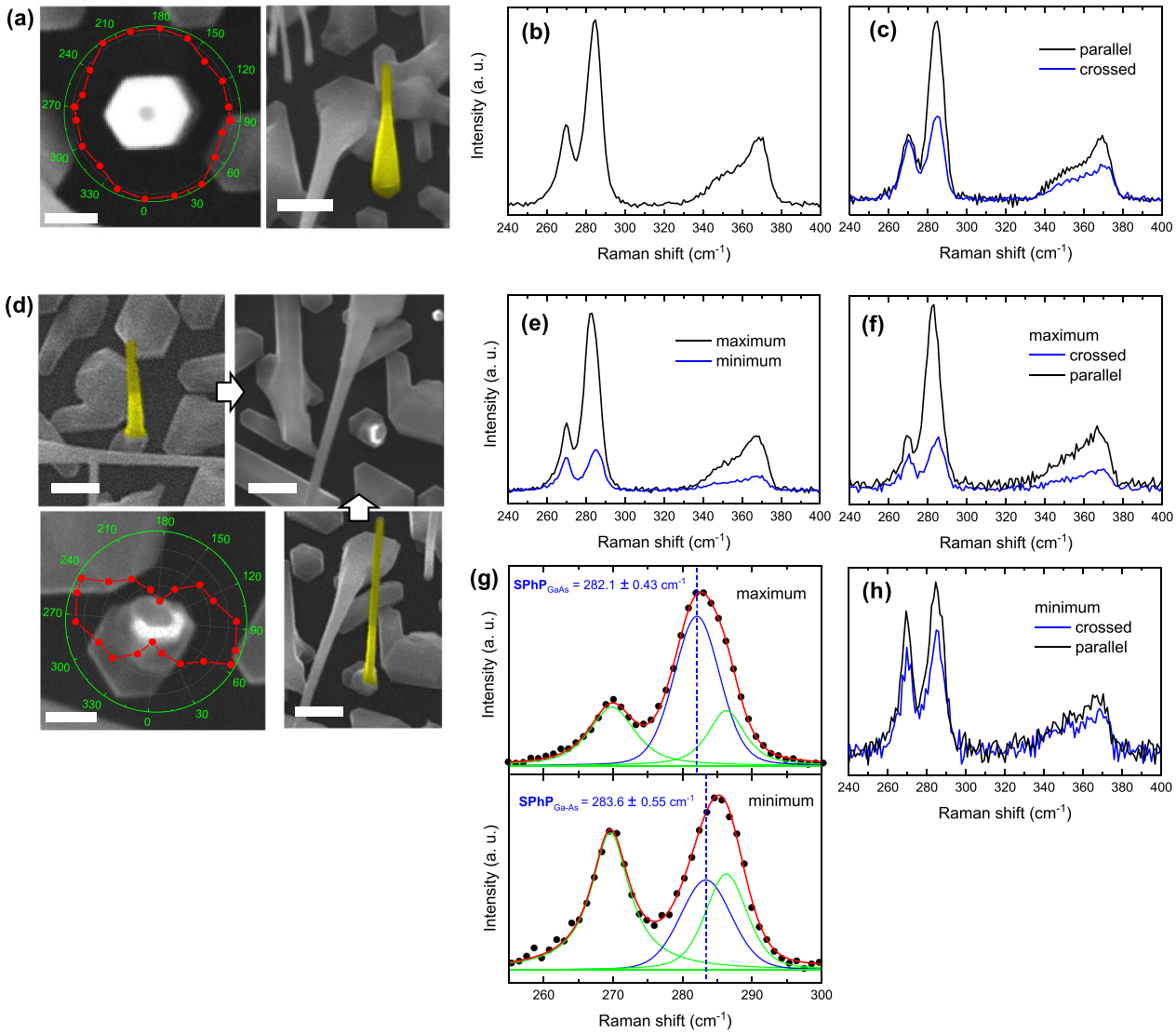

Figure 3. Comparison of hot spots with round (a)–(c) and elongated (d)–(h) cross-sections. (a) In-plane polarisation diagram superimposed on the top-view SEM image of the hot-spot NW of round cross-section (left image, scale bar is 200 nm) and SEM image of the same NW taken at 10° viewing angle (right image, scale bar is 500 nm). (b) Unanalysed spectrum of the hot spot from (a). (c) Spectra of the hot spot from (a) in crossed and parallel polarisations. (d) In-plane polarisation diagram superimposed on the top-view SEM image of the hot-spot NW with elongated cross-section (left bottom image, scale bar is 200 nm) and SEM images of the same NW taken at different viewing angles (top left and bottom right, scale bars are 500 nm) illustrating the flat shape of the NW. (e) Unanalysed spectra obtained at maximum and minimum of the polarisation diagram from (d). (f) Spectra of the hot spot from (d) in crossed and parallel polarisations at maximum of the polarisation diagram. (g) Fitting of the GaAs band of the hot-spot spectra from (e) by Voigt peak functions (green and blue curves). Symbols are experimental data points and red curve is the resulting fit. Varying position of SPhP peak is noted. (h) Spectra of the hot spot from (d) in crossed and parallel polarisations at minimum of the polarisation diagram.

SPhP peak width was significantly larger than that of the bulk modes [39].

Importantly, similar SPhP-like spectral weight redistribution is also observed in the GaP-band of the hot-spot spectra (figure 2(a)). For GaP band, the theory predicts [46] four bulk phonon modes, of which only $LO^{As}{}_{GaP}$ has been tabulated [45] with moderate accuracy ($LO^{As}{}_{GaP} = 369.6 \pm 0.4$ cm^{-1} for $x = 0.28$). Such modal complexity in combination with strong broadening makes fitting of the GaP band not very reliable and hence accurate $SPhP_{GaP}$ value cannot be produced. Figure 2(b) show the fitting example of GaP band and the predicted mode assignment. Despite the inaccurate fit of the GaP band, the fact of synchronous appearance of SPhP contribution in both GaAs and GaP bands allows to rule out any accidental coincidence of these features with contribution from some unaccounted impurity compound like surface oxide.

Raman spectra of the GaAsP hot spots with elongated cross-section demonstrate sensitivity to in-plane orientation of the laser polarisation. Due to the relatively low laser absorption in GaAsP, detailed polarisation series can be conducted on these hot spots. Figures 3(a) and (d) show polarisation diagrams obtained for the hot-spot nanowire of round and

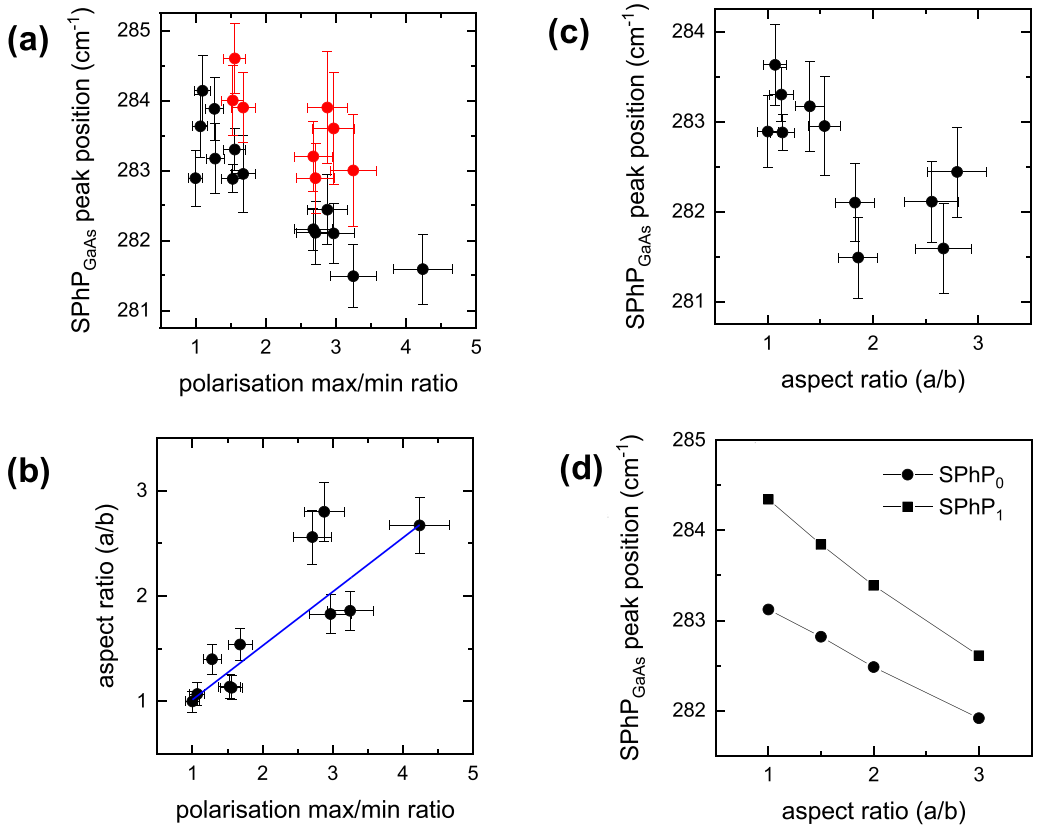

Figure 4. Spectral shift of SPhP peak at different cross-section aspect ratio of hot-spot NW. (a) Fitted SPhP$_{GaAs}$ peak position as function of max/min ratio of the polarisation diagram for different hot spots at maximum (black symbols) and minimum (red symbols) of the polarisation diagram. (b) Correlation of the geometrical cross-section aspect ratio with min/max ratio of the related polarisation diagram. Blue line shows linear regression fit (slope $= 0.51 \pm 0.09$). (c) SPhP$_{GaAs}$ peak position from (a) (black symbols only) replotted as function of the cross-section aspect ratio. (d) Calculated position of SPhP$_0$ and SPhP$_1$ frequencies contributing to experimental SPhP$_{GaAs}$ Raman peak as function of the cross section aspect ratio.

elongated cross-sections, respectively. The diagrams display the integrated unanalysed Raman signal intensity as function of the incident polarisation angle. For the nanowire of round cross-section, no prominent effect of polarisation rotation is observed on the spectral content and intensity (figures 3(a) and (b)). Whereas in case of the elongated cross-section, the maximum of the Raman signal is achieved when the incident laser polarisation is placed along the larger dimension of the nanowire cross-section (figures 3(d) and (e)). Similar correlation has been observed over a number of hot spots as shown in figure S6. It should be noted that no spectral sensitivity to the in-plane polarisation rotation is expected from the bulk Raman scattering tensor of III–V zinc blende crystals for backscattering in <111> direction [48, 49]. Figures 3(e) and (g) compare spectra obtained at the polarisation angles corresponding to minimum and maximum of the polarisation diagram. The spectral difference between these two polarisations is largely due to SPhP$_{Ga\text{-}As}$ peak amplitude variation, which decreases by ~7 times between the maximum and minimum polarisation angles, whereas amplitudes of LO$_{Ga–As}$ and TO$_{Ga–As}$ peaks drop by ~2 times only. Similar trend was observed over a number of hot spots as shown in figure S7 (column ii). Additionally, the position of SPhP$_{Ga–As}$ peak at the maximum is redshifted against that at the minimum (figure 3(g)). The variation of SPhP$_{Ga–As}$ peak position is summarised in figure 4(a) for a number of hot spots. For both polarisation angles, it shows a redshift proportional to maximum/minimum ratio of the polarisation diagram. Adopting the pedestal image of a hot-spot nanowire (shown in figures 3(a), (d) and S6) as a good representation of its cross-section shape, the correlation between the polarisation diagram maximum/minimum ratio and the cross-section geometrical aspect ratio can be established as shown in figure 4(b). This allows for plotting the SPhP$_{Ga–As}$ frequencies as function of the aspect ratio (figure 4(c)). We are not aware of any other study of the NW cross section shape on SPhP properties. The only remotely similar Raman study has been conducted on ZnS nanobelts [38]. In terms of broad NW-related research, the effect of the NW cross section was also noted for polarisation control in NW-based lasers [50].

In addition to the in-plane polarisation rotation, a standard analysis in parallel and crossed polarisers has been conducted for GaAsP hot spots. The results for the different cross-section shapes are shown in figures 3(c), (f) and (h). At the maximum of polarisation diagram, the spectrum is always prominently polarised (figures 3(c) and (f)), and the degree of polarisation ($I_{ll}/I_{\perp}$) is increasing continuously with the cross-section elongation as illustrated by figure S7 (column iii). In contrast, at the minimum intensity condition, the spectra tend to

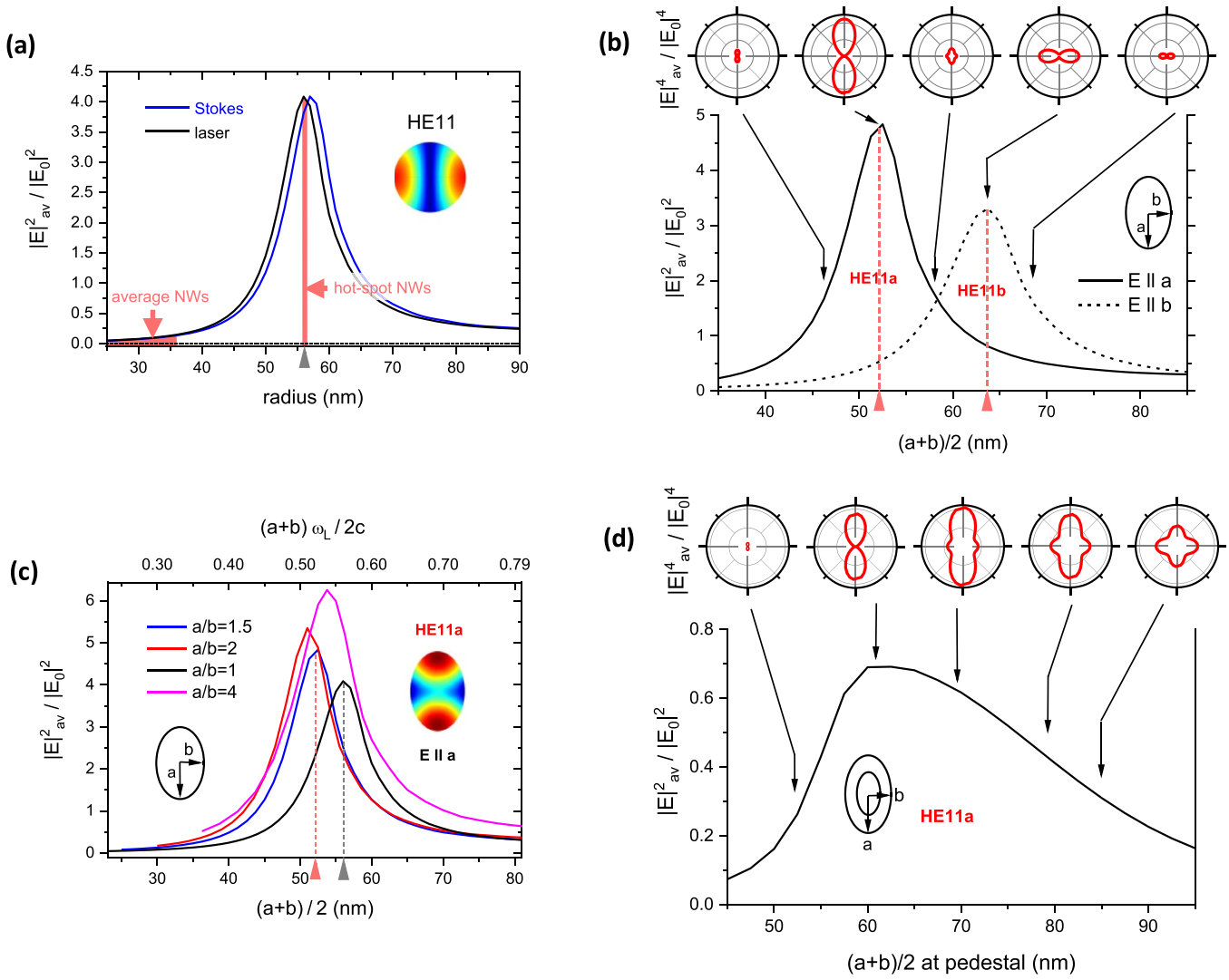

Figure 5. Simulation results. (a) Normalised average squared excitation ($\lambda = 632.8$ nm) and Stokes ($\lambda = 644.6$ nm) electric field norms inside the GaAsP cylinders as function of the cylinder radius. Inserts illustrate HE11 modal electric field distribution at the peak. (b) Normalised average squared excitation electric field norm inside the elliptic ($a/b = 1.5$) GaAsP cylinder as function of the average radius at two different polarisations. Inserts show Raman in-plane polarisation diagrams at different average radius values. (c) Normalised average squared excitation ($\lambda = 632.8$ nm) electric field norm inside the elliptic GaAsP cylinder as function of the average cylinder radius for different a/b aspect ratio at $E\|a$. Upper horizontal scale shows normalised radius values ($\omega_L/c = 2\pi/\lambda$). Inserts illustrate HE11a modal electric field distribution at the peak. (d) Normalised average squared excitation electric field norm at Gaussian beam excitation inside the elliptic ($a/b = 1.5$) GaAsP cone as function of the average pedestal radius at $E\|a$. Inserts show Raman in-plane polarisation diagrams at different pedestal radius values.

be unpolarised (see figures 3(h) and S7 (column iv)). Judging from the GaAs band, the polarisation is largely due to the dominant $SPhP_{GaAs}$ peak, with smaller contribution from LO_{GaAs} and TO_{GaAs} peaks (figures S5(d) and (e)). The $I_{\|}/I_{\perp}$ ratio for $SPhP_{GaAs}$ peak is 2.6 ± 0.3 for the hot spot with the round NW cross-section (figures 3(c) and S5(d)). We are aware of only one report of SPhP Raman peak polarisation measurements in nanowires [37]. The data was obtained on a random GaAs nanowire in the similar backscattering geometry. The polarisation degree ($I_{\|}/I_{\perp}$) of $\approx$2 can be evaluated from the reported data, that is in qualitative agreement with our results. The further detailed comparison is prevented by non-elementary shape of the SPhP peak in [37].

3.3. *Numerical simulations*

Similar enhancement of Raman scattering signal in GaAs nanowires was explained by photonic resonance based on excitation of HE11-like waveguiding modes in nanowires of resonant diameter under employed excitation geometry. Simulation of excitation of $GaAs_{0.72}P_{0.28}$ nanowires confirms the same origin for the hot spot appearance. Indeed, the volume-averaged excitation light intensity inside the 4 μm length $GaAs_{0.72}P_{0.28}$ nanowire shows a resonant dependence from the nanowire radius (figure 5(a)) with peak at $R = 56$ nm. The value of the resonant diameter $2R = 112$ nm is in close agreement to 118.5 ± 20 nm obtained for the mean mid-height

thickness of the hot-spot nanowires. Also, the electric field distribution at the resonance (see insert to figure 5(a)) is typical for HE11 mode.

For quantification of Raman signal enhancement, it will be assumed that both excitation and Raman Stokes components are described by the HE11-like modes. Since the $|E|^2$ vs radius dependence does not change much between the laser and Stokes-shifted wavelengths as shown in the figure 5(a), the variation of the Raman signal can be approximated as variation of the product of $I_{\text{laser}} \times I_{\text{Stokes}} \propto |E_{\text{laser}}|^2 \times |E_{\text{Stokes}}|^2 \approx |E_{\text{laser}}|^4$ (ignoring any modal overlap and Raman tensor effects). In $|E_{\text{laser}}|^4$ approximation, the 20–30 times difference (figure 5(a)) in $|E_{\text{laser}}|^2$ between the peak diameter (112 nm, hot spots) and the average-NW diameter (50–70 nm) transforms into 400–900 times difference in Raman signal, which explains the negligible contribution from the average-diameter NWs in experimental Raman maps.

To simulate the effect of the elongated NW cross-section on the HE11 resonance, the cylinder was changed to an elliptical cylinder. As a result, the excitation efficiency became sensitive to in-plane polarisation of the excitation light. As shown in figure 5(b), the HE11 resonance peak is split into two, reflecting two basic polarisations along the semi axes of the elliptical cross section. For $E\|a$, the excitation field intensity is peaked at slightly lower average radius than that for the circular cylinder (figure 5(c)). At $E\|b$, the resonance appears at larger radius and it is of smaller amplitude. The difference in amplitude and position of the resonance peaks for $E\|a$ and $E\|b$ is further increasing with the a/b aspect ratio. This resonance splitting agrees with the known splitting of HE11 wave-guiding mode in the infinite elliptical cylinder into two HE11-like modes with basic polarisations along the shorter and longer semi-axis [51]. This splitting is reproduced by numerical simulation of the dispersion diagram for GaAsP nonadsorbing infinite elliptical cylinder shown in figure 6(a). The dispersion diagram is calculated for the varied average cylinder radius at fixed excitation wavelength and $a/b = 1.5$ ratio. It shows that HE11b ($E\|b$) mode is shifted up to higher average radius ($(a + b)/2$) values against the HE11a ($E\|a$) branch. The splitting is further increasing with a/b ratio (figure S8(a)), quickly moving HE11b branch outside the practical NW diameter distribution.

Stronger resonance peak at $E\|a$ is in excellent agreement with the experimental results, which consistently showed strongest signal at $E\|a$ condition (figures 3(e) and S6). Moreover, the large variation of $\text{SPhP}_{\text{GaAs}}$ peak intensity between $E\|a$ and $E\|b$ polarisations observed in experiment (figures 3(g) and S7) provides further evidence of connection between the resonance appearance and SPhP peak amplification.

The predicted $|E|^4$ in-plane polarisation diagrams (insert in figure 5(b)) are in qualitative agreement with the experimental data shown in figures 3(d) and S6, confirming that the photonic properties of the flattened waveguide are responsible for the polarisation diagrams observed in experiment. Quantitatively, the simulated diagram signal variations are much stronger than the experimental values for the comparable a/b ratios (figures 3(d) and S6). However, once the simulations have adopted the more realistic conditions including the cone shape and the Gaussian beam excitation, the simulated polarisation diagram min/max ratio becomes significantly weaker (see figure 5(d)) approaching the experimental values.

The flattened waveguide also affects the band polarisation measurements. In particular at $E\|a$ resonance, it supports light propagation with polarisation parallel a and attenuates light polarised along b. This explains the apparent enhancement of the Raman band polarisation ($I_{\text{ll}}/I_{\perp}$ ratio) observed for the hot spots with elongated cross-section (figures 3(c), (f) and S7 (column iii)). This indicates that the true polarisation ratio can be obtained only on NWs of circular cross section.

Adopting HE11 resonance diameters obtained from the finite NW simulations (figure 5(b)), HE11 modal k_z wavevectors can be found from the dispersion diagram as shown in figure 6(a). That obtained k_z values are close to that of the free light dispersion, indicating that electromagnetic field of the excited resonant HE11 modes is still largely distributed outside the nanowire. This agrees with more detailed analysis of HE11 modes in GaAs nanowires [39].

To calculate the expected SPhP frequencies appearing in Raman spectra we adopt the model where both incident and scattered light are propagating as HE11 (or HE11a) modes with k_z parameters indicated in figure 6(a). The dispersion of SPhP modes is calculated in approximation of infinite non-absorbing GaAsP elliptical cylinder by numerical simulation with the cylinder dielectric function represented as:

$$\varepsilon(\omega) = \varepsilon_\infty + \frac{\varepsilon_0 - \varepsilon_\infty}{1 - \left(\frac{\omega}{\omega_{\text{TO}}}\right)^2}, \tag{1}$$

where ε_0 is the static permittivity, ε_∞ is the permittivity at high (optical) frequencies, and ω_{TO} is the transverse optical lattice vibration for zinc-blende GaAsP. Taking $\omega_{\text{TO}} = 269.8\ \text{cm}^{-1}$, $\varepsilon_0 = 11.63$, $\varepsilon_\infty = 10.33$, (equivalent to $\omega_{\text{LO}} = 286.3\ \text{cm}^{-1}$), the dispersion of SPhP modes has been calculated at HE11 (HE11a) resonances. The results for the 1st two modes (SPhP_0 and SPhP_1) obtained for the circular and elliptic ($a/b = 1.5$) cylinders are shown in figure 6(b) (see also figure S8(b)). For the elliptical nanowire, the dipolar SPhP_1 mode is split and the symmetrical SPhP_0 mode is shifted down as compared to the circular nanowire case. The wavevector of SPhP (k_z^{SPhP}), involved in the backscattering Raman geometry, has the twice of k_z value of the involved HE11 mode (ignoring the difference in k_z between the incident and scattered light). For that defined k_z^{SPhP}, the diagram in figure 6(b) gives $\omega_{\text{SPhP0}} = 283.12\ \text{cm}^{-1}$ and $282.82\ \text{cm}^{-1}$ for circular and elliptic cross section respectively. The ω_{SPhP0} and ω_{SPhP1a} values obtained for a range of a/b ratio are plotted in figure 4(d). Both SPhP frequencies (figure 4(d)) show a red shift with a/b ratio, which broadly reproduces the experimental dependence observed in figure 4(c). Since the symmetrical SPhP_0 mode is normally expected [52–54] to produce a dominant contribution to the Raman signal, we compare the calculated SPhP_0 data with experimental $\text{SPhP}_{\text{GaAs}}$ frequencies obtained at $E\|a$. At $E\|b$, the experimental SPhP peak is strongly diminished and blue-shifted by $\sim 1\ \text{cm}^{-1}$ (figure 4(a)), which can be explained by the decreased contribution from SPhP_0 and large relative contribution from SPhP_1. Including SPhP_1 mode

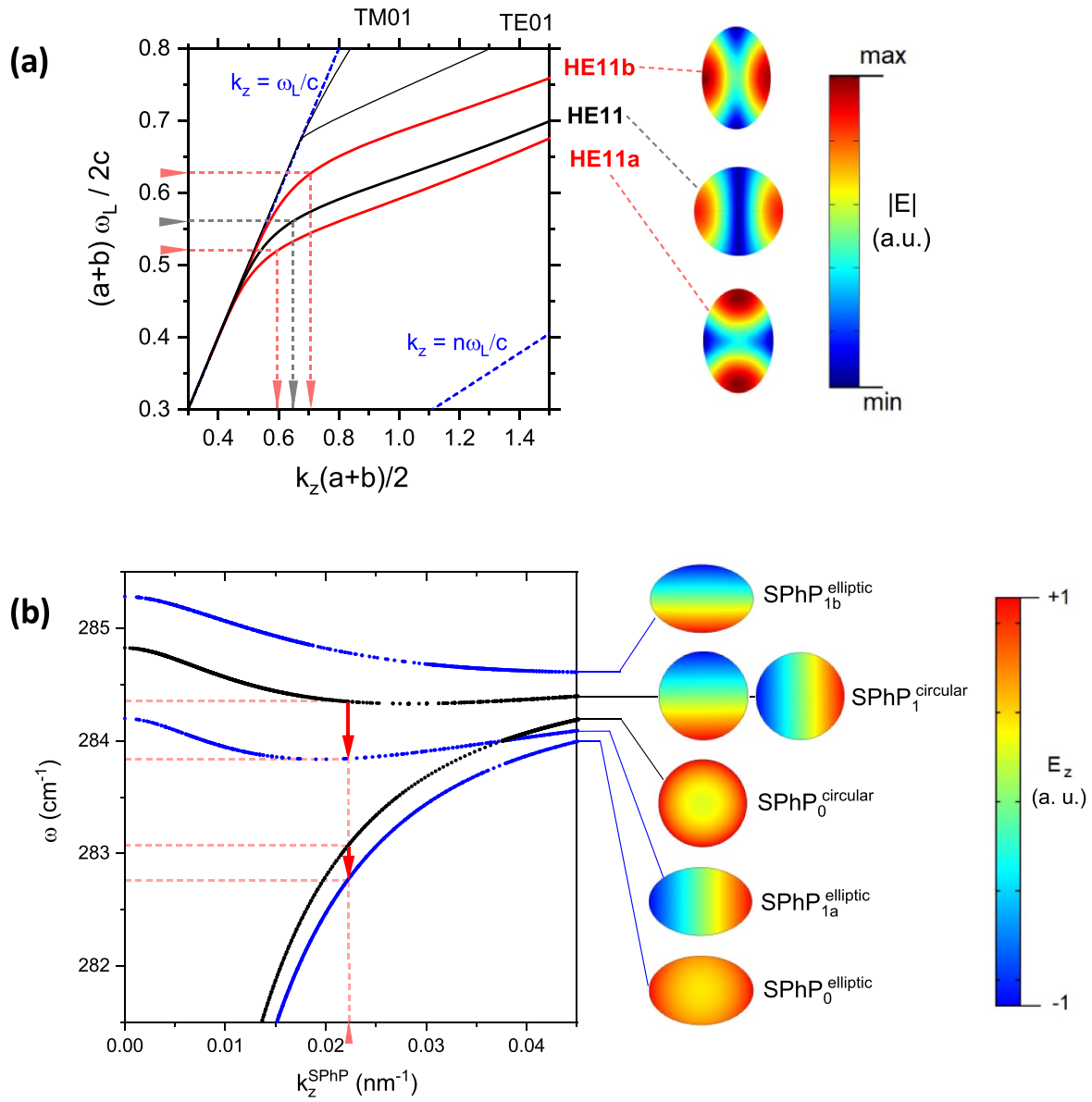

Figure 6. Simulated dispersion diagrams. (a) Dispersion of HE11 waveguiding modes of infinite nonadsorbing GaAsP cylinder in air at $\lambda = 632.8$ nm excitation (corresponding to frequency $\omega_L = 2\pi c/\lambda$) for circular (black) and elliptic (red, $a/b = 1.5$) cylinders. Blue dashed lines indicate light line in air and in GaAsP (refractive index $n = 3.7$). Arrows indicate operating points corresponding to the resonance peaks in figures 5(a) and (b). Inserts illustrate distribution of HE11 modal electric field. (b) Dispersion diagram for the 1st two SPhP modes of nonadsorbing infinite GaAsP cylinders at resonant radius. Black traces show data for the circular-cross section cylinder and blue colour indicate data for the elliptical cylinder with $a/b = 1.5$. Inserts illustrate distribution of SPhP modal electric field. Arrows indicate red shift of SPhP peaks induced by the cross section flattening.

into analysis extends the predicted spectral shift range, which further improve the quantitative agreement with the experimental data. To predict the accurate contribution from two SPhP modes into experimental spectra, the more detailed calculations involving modal overlap will be required.

Since the actual nanowires are hexagonal faceted, we have assessed an effect of the faceting on the NW photonic properties. The obtained results (shown in figure S9) clearly prove a negligible effect of the hexagonal faceting, at least for the NW diameters satisfying the HE11 resonance conditions.

To summarise, the photonic properties of flattened nanowire are responsible for the observed SPhP peak's amplitude and spectral variations at the rotated in-plane polarisation. Control of these properties via engineering of the NW's cross section offers new prospective in SPhP applications in surface and chemical sensors, heat emission and IR micro-photonic.

4. Conclusions

The strong photonic-resonance enhancement of SPhP Raman signal previously observed on GaAs nanowires has been reproduced on GaAsP nanowires. High amplitude of SPhP peak in combination with low laser-induced overheating in GaAsP allowed for the extended studies of SPhP properties on

individual NW level. In particular, the polarisation properties of SPhP and effect of flattening of the NW cross section has been investigated. It was shown that the flattening induces the in-plane polarisation and spectral red shift of SPhP peak. Supporting experimental results analysis with extensive numerical simulations, the observed effects were linked to the transformation of governing HE11 photonic resonance and SPhP dispersion in flattened nanowires. The obtained results create the basis for polarisation control and precise sensing of SPhPs in dielectric nanowires.

Data availability statement

All data that support the findings of this study are included within the article (and any supplementary files).

Acknowledgments

The authors acknowledge the support of Leverhulme Trust, EPSRC (Grant Nos. EP/P000916/1 and EP/P000886/1), and EPSRC National Epitaxy Facility.

Conflict of interest

The authors declare no competing financial interest.

ORCID iDs

Sergey I Rybchenko https://orcid.org/0000-0002-9899-313X
Huiyun Liu https://orcid.org/0000-0002-7654-8553

References

[1] Agranovich V M and Mills D L Modern Problems in Condensed Matter Sciences (eds) 1982 *Surface Polaritons: Electromagnetic Waves at Surfaces and Interfaces* 1 (Amsterdam: North-Holland Publishing Company)
[2] Caldwell J D *et al* 2015 Low-loss, infrared and terahertz nanophotonics using surface phonon polaritons *Nanophotonics* **4** 44–68
[3] Berte R, Gubbin C R, Wheeler V D, Giles A J, Giannini V, Maier S A, de Liberato S and Caldwell J D 2018 Sub-nanometer thin oxide film sensing with localized surface phonon polaritons *ACS Photonics* **5** 2807–15
[4] Autore M *et al* 2018 Boron nitride nanoresonators for phonon-enhanced molecular vibrational spectroscopy at the strong coupling limit *Light Sci. Appl.* **7** 17172
[5] Francescato Y, Giannini V, Yang J, Huang M and Maier S A 2014 Graphene sandwiches as a platform for broadband molecular spectroscopy *ACS Photonics* **1** 437–43
[6] Herrera F and Owrutsky J 2020 Molecular polaritons for controlling chemistry with quantum optics *J. Chem. Phys.* **152** 100902
[7] Feist J, Galego J and Garcia-Vidal J F 2018 Polaritonic chemistry with organic molecules *ACS Photonics* **5** 205–16
[8] Bylinkin A *et al* 2021 Real-space observation of vibrational strong coupling between propagating phonon polaritons and organic molecules *Nat. Photon.* **15** 197–202
[9] Caldwell J D, Lindsay L, Giannini V, Vurgaftman I, Reinecke T L, Maier S A and Glembocki O J 2015 Low-loss, infrared and terahertz nanophotonics using surface phonon polaritons *Nanophotonics* **4** 44–68
[10] Foteinopoulou S, Devarapu G C R, Subramania G S, Krishna S and Wasserman D 2019 Phonon-polaritonics: enabling powerful capabilities for infrared photonics *Nanophotonics* **8** 2129–75
[11] Feng K, Streyer W, Zhong Y, Hoffman A J and Wasserman D 2015 Photonic materials, structures and devices for reststrahlen optics *Opt. Express* **23** A1418–33
[12] Greffet J J, Carminati R, Joulain K, Mulet J-P, Mainguy S and Chen Y 2002 Coherent emission of light by thermal sources *Nature* **416** 61–64
[13] Song J, Cheng Q, Zhang B, Lu L, Zhou X, Luo Z and Hu R Many-body near-field radiative heat transfer: methods, functionalities and applications 2021 *Rep. Prog. Phys.* **84** 036501
[14] Lucchesi C, Vaillon R and Chapuis P-O 2021 Radiative heat transfer at the nanoscale: experimental trends and challenges *Nanoscale Horiz.* **6** 201–8
[15] Chen D-Z A, Narayanaswamy A and Chen G 2005 Surface phonon-polariton mediated thermal conductivity enhancement of amorphous thin films *Phys. Rev.* B **72** 155435
[16] Li W and Fan S 2018 Nanophotonic control of thermal radiation for energy applications *Opt. Express* **26** 15995
[17] Li W, Buddhiraju S and Fan S 2020 Thermodynamic limits for simultaneous energy harvesting from the hot sun and cold outer space *Light Sci. Appl.* **9** 68
[18] Zou Y, Chakravarty S, Chung C-J, Xu X and Chen R T 2018 Mid-infrared silicon photonic waveguides and devices *Photonics Res.* **6** 254
[19] Alessandri I and Lombardi J R 2016 Enhanced Raman scattering with dielectrics *Chem. Rev.* **116** 14921–81
[20] Koshelev K and Kivshar Y 2021 Dielectric resonant metaphotonics *ACS Photonics* **8** 102–12
[21] Raza S and Kristensen A 2021 Raman scattering in high-refractive-index nanostructures *Nanophotonics* **10** 1197–209
[22] Romano S, Zito G, Managò S, Calafiore G, Penzo E, Cabrini S, de Luca A C and Mocella V 2018 Surface-enhanced Raman and fluorescence spectroscopy with an all-dielectric metasurface *J. Phys. Chem.* C **122** 19738–45
[23] Ushioda S, Aziza A, Valdez J B and Mattei G 1979 Effects of surface roughness on surface polaritons *Phys. Rev.* B **19** 4012
[24] Mattei G, Pagannone M, Fornari B and Mattioli L 1982 Surface polariton dispersion measurement by Raman scattering excited in total reflection condition *Solid State Commun.* **44** 1495–8
[25] Denisov V N, Mavrin B N and Podobedov V B 1987 Raman scattering by surface polaritons in a gap crystal: dispersion, intensity, and polarization properties *Sov. Phys. JETP* **65** 1042–9
[26] Evans D J, Ushioda S and McMullen J D 1973 Raman scattering from surface polaritons in a GaAs film *Phys. Rev. Lett.* **31** 369
[27] Davydov V Y, Subashiev A V, Cheng T S, Foxon C T, Goncharuk I N, Smirnov A N and Zolotareva R V 1997 Raman scattering by surface polaritons in cubic GaN epitaxial layers *Solid State Commun.* **104** 397–400
[28] Nga S S, Yoon T L, Hassan Z and Abu Hassan H 2009 Surface and interface phonon polaritons of wurtzite GaN thin film grown on 6H-SiC substrate *Appl. Phys. Lett.* **94** 241912
[29] Prasad N and Karthikeyan B A 2019 Raman spectral probe on polar w-ZnS nanostructures and surface optical phonon modes in nanowires *Nanoscale* **11** 4948–58

[30] Mata R, Cross A, Hestroffer K and Daudin B 2012 Surface optical phonon modes in GaN nanowire arrays: dependence on nanowire density and diameter *Phys. Rev.* B **85** 035322
[31] García Núñez C, Braña A F, Pau J L, Ghita D, García B J, Shen G, Wilbert D S, Kim S M and Kung P 2014 Surface optical phonons in GaAs nanowires grown by Ga-assisted chemical beam epitaxy *J. Appl. Phys.* **115** 034307
[32] Gupta R, Xiong Q, Mahan G D and Eklund P C 2003 Surface optical phonons in gallium phosphide nanowires *Nano Lett.* **3** 1745–50
[33] Spirkoska D, Abstreiter G and I Morral A F 2008 Size and environment dependence of surface phonon modes of gallium arsenide nanowires as measured by Raman spectroscopy *Nanotechnology* **19** 435704
[34] Watt M, Sotomayor Torres C M, Arnot H E G and Beaumont S P 1990 Surface phonons in GaAs cylinders *Semicond. Sci. Technol.* **5** 285–90
[35] Walia J, Dhindsa N, Flannery J, Khodabad I, Forrest J, LaPierre R and Saini S S 2014 Enhanced photothermal conversion in vertically oriented gallium arsenide nanowire arrays *Nano Lett.* **14** 5820–6
[36] Wu J, Gupta A K, Gutierrez H R and Eklund P C 2009 Cavity-enhanced stimulated raman scattering from short GaP nanowires *Nano Lett.* **9** 3252–7
[37] Speiser E, Hinrichs K, Prete P, Lovergine N and Esser N 2015 Vibrational Raman scattering from surfaces of III–V semiconductors: microscopic and macroscopic surface modes *Phys. Status Solidi* b **252** 11–18
[38] Ho C, Varadhan P, Wang H, Chen C, Fang X and He J 2016 Raman selection rule for surface optical phonons in ZnS nanobelts *Nanoscale* **8** 5954–8
[39] Rybchenko S I, Ali S, Zhang Y and Liu H 2021 Resonant enhancement of Raman scattering by surface phonon polaritons in GaAs nanowires *J. Phys. D: Appl. Phys.* accepted (https://doi.org/10.1088/1361-6463/ac1a32)
[40] Crark G D and Holonyak N 1967 Optical properties of gallium arsenide-phosphide *Phys. Rev.* **156** 913
[41] Aspnes D E and Studna A A 1983 Dielectric functions and optical parameters of Si, Ge, GaP, GaAs, GaSb, InP, InAs, and InSb from 1.5–6.0 eV *Phys. Rev.* B **27** 985–1009
[42] Hasegawa S, Tanaka A and Sukegawa T 1984 Optical absorption coefficient near fundamental absorption edge of GaAsP *J. Appl. Phys.* **55** 3188–9
[43] Holm J, Jørgensen H I, Krogstrup P, Nygård J, Liu H and Aagesen M 2013 Surface-passivated GaAsP single-nanowire solar cells exceeding 10% efficiency grown on silicon *Nat. Commun.* **4** 1498
[44] Zhang Y and Liu H 2020 Self-catalyzed GaAs (P) nanowires and their application for solar cells *J. Phys. D: Appl. Phys.* **53** 233001
[45] Pistol M-E and Liu X 1992 Quantum-well structures of direct-band-gap $GaAs_{1-x}P_x$/GaAs studied by photoluminescence and Raman spectroscopy *Phys. Rev.* B **45** 4312
[46] Pages O, Souhabi J, Postnikov A V and Chafi A 2009 Percolation versus cluster models for multimode vibration spectra of mixed crystals: GaAsP as a case study *Phys. Rev.* B **80** 035204
[47] Im H S, Jung C S, Park K, Jang D M, Lim Y R and Park J 2014 Band gap tuning of twinned GaAsP ternary nanowires *J. Phys. Chem.* C **118** 4546–52
[48] Puech P, Landa G, Carles R and Pizani P S 1994 Raman scattering study of [hhk]-GaAs/(Si or CaF_2) strained heterostructures *J. Appl. Phys.* **76** 2773
[49] Steele J A, Puech P and Lewis R A 2016 Polarized Raman backscattering selection rules for (hhl)-oriented diamond- and zincblende-type crystals *J. Appl. Phys.* **120** 055701
[50] Foster A P, Bradley J P, Gardner K, Krysa A B, Royall B, Skolnick M S and Wilson L R 2015 Linearly polarized emission from an embedded quantum dot using nanowire morphology control *Nano Lett.* **15** 1559–63
[51] Yen C 1962 Elliptical dielectric waveguides *J. Appl. Phys.* **33** 3235
[52] Ruppin R and Englman R 1970 Optical phonons of small crystals *Rep. Prog. Phys.* **33** 149–96
[53] Ruppin R 1975 Thermal fluctuations and Raman-scattering in small spherical crystals *J. Phys.* C **8** 1969
[54] Ruppin R and Englman R 1969 Rayleigh and Raman Scattering by Surface Modes in Ionic Crystals *Light Scattering Spectra of Solids* ed G B Wright (*New York University, New York, September 3–6, 1968*)